Journal of Colloid and Interface Science 575 (2020) 274–285

Contents lists available at ScienceDirect

Journal of Colloid and Interface Science

journal homepage: www.elsevier.com/locate/jcis

Monte Carlo Aggregation Code (MCAC) Part 2: Application to soot agglomeration, highlighting the importance of primary particles

J. Morán [a], J. Yon [a,*], A. Poux [a], F. Corbin [a], F.-X. Ouf [b], A. Siméon [c]

[a] Normandie Université, INSA Rouen, UNIROUEN, CNRS, CORIA, 76000 Rouen, France
[b] Institut de Radioprotection et de Sûreté Nucéaire (IRSN), PSN-RES, SCA, Gif-Sur-Yvette 91192, France
[c] Université de Lille, CNRS, UMR 8518 – LOA – Laboratoire d'Optique Atmosphérique, 59000 Lille, France

HIGHLIGHTS

- Both nearest-neighbor and fluid Knudsen numbers must be considered.
- Fractal dimension is dependent on primary particles size.
- A new and robust method to calculate the homogeneity coefficient is proposed.
- Self-preserving size distribution is a generalized Gamma distribution.

GRAPHICAL ABSTRACT

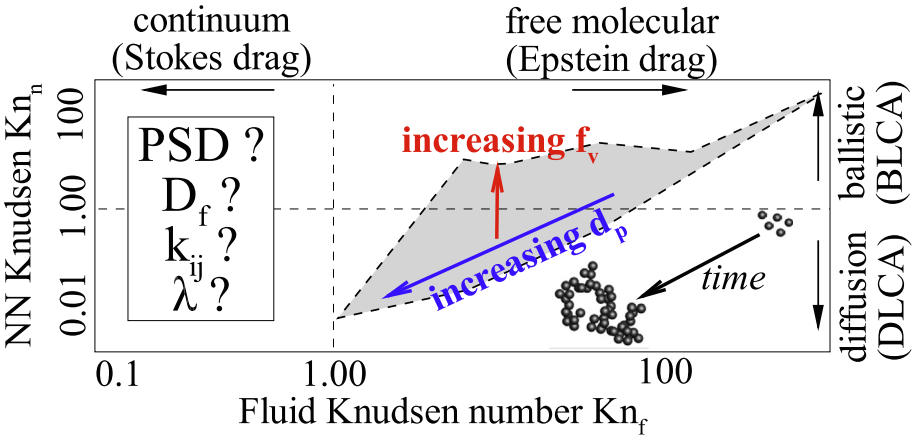

ARTICLE INFO

Article history:
Received 18 February 2020
Revised 19 April 2020
Accepted 20 April 2020
Available online 28 April 2020

Keywords:
Diffusive and ballistic agglomeration
Primary particles
Flow regime
Fractal dimension
Soot

ABSTRACT

During the agglomeration of nanoparticles and in particular, soot, a change in both the flow regime (from free molecular to near continuum) as well as the change of agglomeration regime (from ballistic to diffusive) is expected. However, these effects are rarely taken into account in numerical simulations of particle agglomeration and yet, they are suspected to have an important impact on the agglomeration kinetics, particle morphologies, and size distributions. This work intends to study these properties by using the Monte Carlo Aggregation Code (MCAC) presented in the preceding work (part 1), focusing on the physical impacts of varying the particle volume fraction and monomers size and polydispersity. The results show an important sensitivity of the kinetics of agglomeration, coagulation homogeneity, and agglomerate morphology to the size of monomers. First, for smaller monomer diameters, the agglomeration kinetic is enhanced and agglomerates are characterized by larger fractal dimensions. Second, for large monomer diameters, fractal dimensions down to 1.67 can be found being smaller than the classical 1.78 for Diffusion Limited Cluster Agglomeration (DLCA) mechanism. One important conclusion is that variation in time of both regimes has to be considered for a more accurate simulation of the agglomerate size distribution and morphology.

* Corresponding author.
E-mail address: yon@coria.fr (J. Yon).

https://doi.org/10.1016/j.jcis.2020.04.085
0021-9797/

Nomenclature

α	Arbitrary constant value (–)
Δt	Time step associated with the particle persistent distance (s)
Γ	Gamma function (–)
λ	Coagulation homogeneity coefficient (–)
λ_f	Fluid mean free path (m)
λ_p	Particle's persistent distance (m)
λ_{Mi}	Coagulation homogeneity coefficient based on the i'th moment of the size distribution (–)
ρ_p	Particle bulk mass density ($\mathrm{kg{\cdot}m^{-3}}$)
$\sigma_{geo,d}$	Particle geometric standard deviations based on the diameter d (–)
$\sigma_{geo,p}$	Primary particle geometric standard deviation (–)
τ	Particle momentum relaxation time (s)
τ_a	Characteristic time of agglomeration (μs)
τ_{cs}	Characteristic time of coagulation for coalescing spheres (μs)
$\tilde{x}$	Average particle size parameter for the Self-Preserving Size Distribution (m)
a	Generalized gamma Self-Preserving Size Distribution parameter (–)
D	Particle diffusion coefficient ($\mathrm{m^2{\cdot}s^{-1}}$)
d	Generalized gamma Self-Preserving Size Distribution parameter (–)
D_f	Particle mass fractal dimension (–)
d_g	Particle gyration diameter (m)
d_m	Particle mobility diameter (m)
d_p	Primary particle diameter (nm)
d_v	Particle volume equivalent diameter (m)
D_{fm}	Mobility based fractal dimension (–)
f	Agglomerate friction coefficient ($\mathrm{kg{\cdot}s^{-1}}$)
f_v	Particle volume fraction (–)
H	Dimensionless coagulation kernel (–)
$k(i,j)$	Coagulation kernel between ith and jth particles ($\mathrm{m^3{\cdot}s^{-1}}$)
k_0	Average monomer coagulation kernel ($\mathrm{m^3{\cdot}s^{-1}}$)
k_B	Boltzmann constant ($\mathrm{m^2{\cdot}kg{\cdot}s^{-2}{\cdot}K^{-1}}$)
n	Particle number concentration ($\mathrm{m^{-3}}$)
n_0	Initial particle number concentration ($\mathrm{m^{-3}}$)
N_p	Number of primary particles per agglomerate (–)
p	Generalized gamma Self-Preserving Size Distribution dimension parameter (–)
p_i	Probability of the ith particle displacement, $i \in [1, N_p]$ (–)
q	Order of the moments of the particle size distribution (–)
r_m	Particle mobility radius (m)
Kn_n	Nearest-neighbor Knudsen number (–)
r_{max}	Average particle maximum radius (m)
$R_{s,ij}$	Relative collision or Smoluchowski radius (m)
T	Absolute temperature (K)
t	Time (s)
v	Particle volume ($\mathrm{m^3}$)
X	Dimensionless particle size parameter for the Self-Preserving Size Distribution (–)
x	Particle size parameter for the Self-Preserving Size Distribution (m)
z	Kinetic exponent (–)
Kn_D	Diffusive Knudsen number (–)
Kn_f	Fluid Knudsen number (–)
PA_{ij}	Relative particle projected area ($\mathrm{m^2}$)
r_n	Nearest-neighbor distance (m)

1. Introduction

The agglomeration of suspended nanoparticles is a phenomenon of great complexity but also of great common interest in both aerosol and colloid systems. Both terms agglomerate and aggregate are usually encountered with a confusing interchange. In the present document, the terms agglomerate/agglomeration are used as recommended by [1]. In this process of agglomeration, particles naturally evolve into complex fractal-like morphology of polydisperse size consisting also of polydisperse primary particles. Eventually, depending on the physical conditions, particles may change the way they interact with the surrounding fluid and also the way they interact with each other. In other words, particles may undergo a change of flow regime and/or agglomeration regime, respectively. The flow regime is characterized by the classical fluid Knudsen number $Kn_f = \lambda_f / r_m$, where λ_f and r_m are the fluid mean free path and the particle mobility radius, respectively. Here, λ_f is the average distance travelled by fluid molecules between successive collisions and r_m is the radius of a sphere that perceives the same drag force as the agglomerate [2]. When Kn_f tends toward 0, the relevant hydro/aerodynamic forces result from a continuous process (continuum regime), whereas at large Kn_f they are related to discrete collisions with molecules (free molecular regime). As introduced by Pierce et al. [3], the agglomeration regime can be quantified by the nearest-neighbor Knudsen number $Kn_n = \lambda_p / r_n$, where $\lambda_p = \sqrt{18 D \tau}$ is the particle persistent distance [4] calculated from the particle diffusion coefficient D and momentum relaxation time $\tau = m/f$. The latter corresponds to the ratio between particle mass and friction coefficient. λ_p is the distance over which particles experience an approximately ballistic movement [3]. r_n is the nearest-neighbor distance and is given by $r_n = n^{-1/3} - 2r_{max}$ where n is the particle number concentration and r_{max} is the average maximum radius describing the agglomerate.

When Kn_n is high, cluster agglomeration tends to become ballistically limited (i.e. BLCA) whereas when tending toward 0, it is diffusion-limited (i.e. DLCA). For soot particles generated in premixed or diffusion flames, the fluid Knudsen number has been typically considered with $Kn_f \gg 1$, i.e. being in the free molecular regime [5–7], meanwhile other studies have shown it can evolve down to $Kn_f \sim 1$ depending on the flame conditions [8]. Moreover, for different aerosol and colloid systems, fluid Knudsen numbers up to $Kn_f \sim 10$ have been found in the transition regime for titania and silica aerosols [9], oleic acid and sodium chloride aerosols [10,11], di(2-ethylhexyl) sebacate in a rarefied gas [12] and down to $Kn_f \sim 0.1$ by other studies involving different types of particles [13–16].

Fig. 1 summarizes most of the current simulations found in the literature as classified based on the above mentioned Knudsen numbers. Agglomeration has been commonly studied in the continuum flow regime for diffusion-limited agglomeration (DLCA + Stokes drag) [17,18]. Indeed, in this context, the transition from strong inter-particle interactions forces, i.e. DLCA to the weak interactions (reaction limited agglomeration, RLCA) has been studied [17–20]. In the present work, focused on soot particle agglomeration, strong interaction forces are considered and therefore the transition towards the RLCA regime is beyond the scope of this article. Pierce et al. [3] studied the DLCA with an Epstein drag. Transition in the flow regimes (abscissa in Fig. 1) is complex due to the lack of models for calculating the friction coefficient of

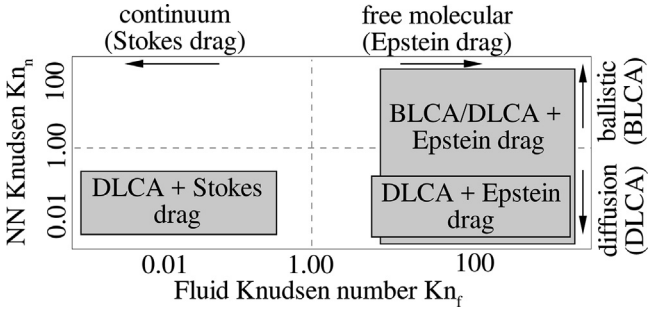

Fig. 1. Different regimes of agglomeration and fluid flow studied in the literature.

fractal agglomerates. In this context, some studies have treated both continuum and free molecular flow regimes separately [21]. Similarly, BLCA and DLCA are generally treated independently [17]. Notably, only a few studies have considered a transition between both agglomeration regimes (vertical axis in Fig. 1) but commonly in the free molecular flow regime, i.e. with an Epstein drag [22,23]. To the author's knowledge, simultaneous transitions between both agglomeration and flow regimes have not been considered in the past except notably, the work of Thajudeen et al. [24]. The latter is based on Langevin Dynamics simulations by considering the agglomerate morphology, which is very accurate but computationally expensive. However, the influence of the nearest-neighbor distance, the kinetics of agglomeration, the particle size distribution and particle morphology were not systematically studied. The Monte Carlo Aggregation Code (MCAC), developed and validated in the previous work (Part 1 [4]) enables this gap to be covered with a reduced computational cost. In this context, the focus is on the effect of particle volume fraction, and primary particle size and polydispersity. The term aggregation is preferred in the name of the code (MCAC) in accordance with previous similar developments (DLCA/BLCA/RLCA/Tunable aggregation codes). This is also explained by its future goal of simulating strongly connected/overlapping structures (hard agglomerates). Nevertheless, MCAC is used here to study point-touching primary particles, i.e. soft agglomerates [1]. The present work aims to illustrate that caution has to be taken regarding the change in both regimes because they impact the kinetics of agglomeration, particle size distribution, and agglomerate morphology. On the one hand, when increasing the particle volume fraction (f_v), the mean distance between particles decreases and therefore Kn_n increases. Thus, the agglomeration becomes more ballistic and therefore an increase in the fractal dimension of agglomerates has been observed [25]. This is consistent with classical DLCA and BLCA regimes [17], but in the present study, the transition between both regimes is continuous. On the other hand, when the primary particle diameter increases (for example during aggregation or agglomeration and surface growth process), the flow regime evolves. In the context of soot simulation, the agglomeration process is often restricted to the Epstein flow regime because of the high flame temperatures. Nevertheless, from nascent soot typically around 1–4 nm at flame temperatures to the mature primary particles around 30–40 nm eventually released to the atmosphere, the flow regime strongly evolves [26–29].

Another objective of the present study is to analyze and report the evolution of the coagulation kernels during the agglomeration process. Indeed, the Smoluchowski (or population balance) equation has been proved to be a powerful tool for modeling soot agglomeration [29–31]. This equation follows the evolution of the particle number concentration as a function of time. To this end, $k(i,j)$ has to be known, i.e. the coagulation kernels determining the rate of collisions between particles i and j. In certain cases, especially for fractal agglomerates, this kernel is a homogeneous function, i.e. $k(\alpha i, \alpha j) = \alpha^{\lambda} k(i,j)$ where λ is the agglomeration kernel homogeneity parameter. This λ parameter is very important for the kinetics of agglomeration and the resulting particle size distribution qualified as "self-preserving" [32,7]. It has been proposed that λ depends on both the fluid Knudsen number and the nearest-neighbor Knudsen number [3,22], however, these relations are not well understood especially in the transition regime. Considering its simplicity, the scaling hypothesis is widely used to obtain λ [17,9,33,34]. However, its accuracy is rarely discussed [35]. In the present work, a robust and more direct method for determining λ is proposed.

2. Numerical simulations

The algorithm used here has been introduced in the preceding work [4] and therefore, it is described here only briefly. Agglomeration of initially monodisperse or polydisperse spherical primary particles is simulated by using a model based on the classical DLCA mechanism [17], corresponding to the family of Discrete Element Methods [4]. It starts with a total of 3200 randomly placed monomers in a cubic box, ending when the average number of monomers per agglomerate is 100 [36]. Particles are displaced by following the individual positions in time. At each time iteration, particles are displaced individually in a random direction along the persistent distance $\lambda_p = \sqrt{18D\tau}$. The corresponding physical time step is $\Delta t = 3\tau$. As discussed in [4], this time step ensures accurate modeling of agglomeration by Monte Carlo simulations. If the displaced particle collides with a neighboring one, they irreversibly stick together. Otherwise, a new particle is randomly selected in an iterative way. The probabilities p_i for selecting and displacing a particle i are based on the individual time steps Δt_j of all the particles based on the relation $p_i = \Delta t_i^{-1} / \sum_j \Delta t_j^{-1}$. This ensures that the whole population of particles evolves with statistically equivalent residence time [4]. Both, the probabilities of particle displacements and the persistent distances of individual particles, depend on the friction coefficient. To consider the possible change in flow regime due to agglomeration, the method proposed by Yon et al. [37] is used, consisting of a power-law between the agglomerate friction coefficient and the number of constituting primary particles. This model gives physical importance to the primary particle number and diameter in the evaluation of the friction coefficient. It also enables a mobility radius r_m of the agglomerates to be determined by considering their size, morphology, and change in flow regime. Finally, periodic boundary conditions are applied to avoid artificial effects due to the interaction between particles and the containing box. Additionally, when the number of agglomerates is reduced by a factor of eight then, each side of the box is duplicated and the number of agglomerates is increased by a factor of 8. The new agglomerates correspond to periodic images of the existing ones, ensuring a constant particle volume fraction while not influencing the agglomeration process [38,39].

In the present study, a constant primary particle bulk density $\rho_p = 1.8$ g/cm^3 is considered, corresponding to soot particles with low organic content [40]. Three different monomer diameters are simulated, i.e. 1, 20 and 80 nm. Unless indicated, they all consist of monodisperse monomers ($\sigma_{geo,p} = 1$). For the case of polydisperse monomers, a lognormal distribution is considered ($\sigma_{geo,p} = 2$). Particles are suspended in air at a temperature of 1700 K and pressure of 101.3 kPa, corresponding to flame conditions [41]. Three different volume fractions are simulated: 1, 10, and 10^4 ppm. Under these conditions, the fluid mean free path has a constant value of $\lambda_f = 498$ nm, this value is only dependent on fluid temperature and pressure [37]. On the other hand, the

average primary particle persistence distance goes from $\lambda_p = 183$ nm for monomers having $d_p = 20$ nm and $\sigma_{geo,p} = 2$ up to around $\lambda_p = 2000$ nm for monomers having $d_p = 2$ nm. The latter is dependent on the diffusion coefficient and momentum relaxation time of the particles [4].

Except for the highest volume fraction 10^4 ppm (selected for being important for many colloid/aerosol applications [42–45]), these parameters were selected for representing soot particles generated under different combustion systems [26,28,41,46,47]. All the results are averaged over 10 different simulations and error bars reported in figures correspond to the 95% confidence intervals.

3. Results and discussion

3.1. Agglomeration and fluid flow regimes

Fig. 2 illustrates the main advantages of MCAC, i.e. to consider both the time-evolving agglomeration regime (nearest-neighbor Knudsen number Kn_n) and time-evolving fluid flow regime (fluid Knudsen number Kn_f). This figure has the same axes as Fig. 1, but now illustrates the different cases simulated. It clearly shows the ability of MCAC to simulate the evolution in this bidimensional map, indicating that the transition from ballistic to diffusive and from free molecular to near continuum regimes are well taken into account. This simultaneous transition is not commonly considered in the literature.

Initially, particles consist of isolated primary particles (top right position for each case). The initial primary particle diameter and fluid thermodynamic properties determine the horizontal position of this starting point, whereas particle volume fraction and primary particle diameter determine the initial vertical position. As time progresses and agglomerates are growing, thus both Kn_n and Kn_f are decreasing.

By comparing Fig. 2(a) and (b), it is observed that an acceptable variation of the monomer diameters (for soot particles) seems to have a stronger influence on both regimes than a large variation of the volume fraction. Except for the largest particle volume fraction, i.e. 10^4 ppm, the trends are generally related in a power-law with a constant exponent. In the particular case of $f_v = 10^4$ ppm, the system never reaches the diffusive regime since the nearest-neighbor distance is in competition with the fast increase of agglomerate size. This is interpreted as a trend towards the gelling process [33], being outside the scope of this work.

3.2. Kinetics of agglomeration

Fig. 3(a-b) shows the time evolution of the inverse particle number concentration $n(t)$, consisting of the number of particles divided by the volume of the containing box. Due to agglomeration, $1/n(t) - 1/n(0)$ is naturally increasing in time. At short times, when particles are small enough to be treated as spheres, the behavior is approximately linear as predicted by coalescing spheres theory [48] (represented by the black dash-dotted lines, i.e. $1/n(t) - 1/n(0) = (t/\tau_a)^z$ with $z = 1$). This behavior is used to determine τ_a as the exponent of the intercept from the log-log plot of $1/n(t) - 1/n(0)$ as a function of time. The calculated values are reported in Table 1 and compared with the theoretical ones (τ_{cs}). The latter are determined as $\tau_{cs} = 2/(k_0 n_0)$, where $n_0 = n(0)$ is the initial particle number concentration and k_0 is the coagulation kernel of coalescing spheres taking into account the change in flow regime [49], calculated based on the monomer diameters. This parameter is now used to normalize the time on the horizontal axis, thus, enabling this axis to be standardized for the different curves presented. Indeed, the larger τ_a is, the longer the agglomeration process takes. This characteristic time is strongly affected by the variation of f_v and d_p. Nevertheless, both, τ_{cs} and τ_a are on the same order of magnitude except for the largest particle volume fraction (i.e. 10^4 ppm or 1%). Indeed, for this case, τ_{cs} is no longer accurate for predicting real coagulation efficiency [21,42,50]. The above-mentioned combination of $z \to 1$ and $\tau_a \approx \tau_{cs}$ ensures that there is a reliable simulation of the agglomeration kinetics by MCAC, at least for short times. For longer times corresponding to larger particles, due to the agglomerate morphology, the behavior tends to a power law $1/n(t) - 1/n(0) = (t/\tau_a)^z$, where z is the kinetic exponent that may be different from 1, and its value depends on the agglomeration and flow regimes [3,21]. These values are shown in Fig. 3 and reported in Table 1. Kinetics of agglomeration is enhanced (z increases) when increasing the volume fraction or decreasing the monomer diameters. The largest value is found for $d_p = 1$ nm, corresponding to ballistic agglomeration (the largest Kn_n in Fig. 3(b)). This is in very good agreement with Pierce et al. [3] who reported an asymptotic value of $z = 2.2$ in this regime compared to 2.17 found in the present study. When

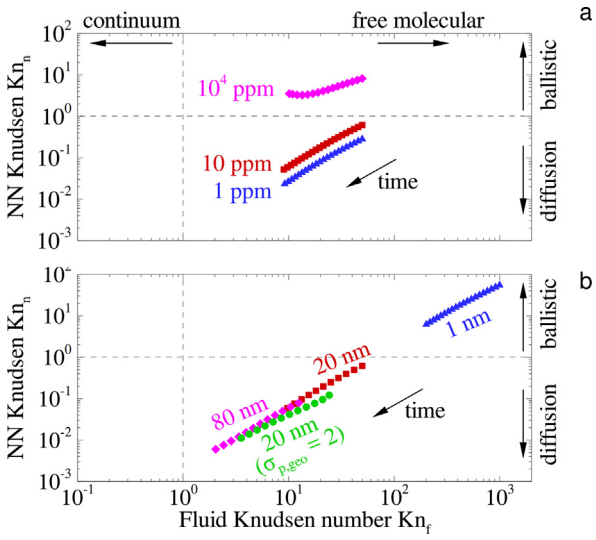

Fig. 2. Different regimes of agglomeration and fluid flow for (a) different particle volume fraction and (b) different monomer diameters.

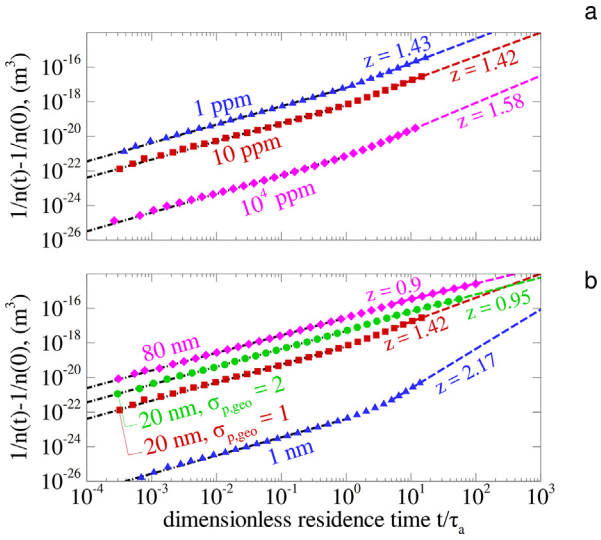

Fig. 3. Inverse number concentration as a function of the normalized residence time. The τ_a stands for the characteristic time of agglomeration.

Table 1
Parameters for the analysis of agglomeration kinetics at short and long times.

Case	Short times		Long times		
	τ_a (μs)	τ_{cs} (μs)	z	Kn_f*	Kn_n*
f_v (ppm)					
1	1191	1262	1.43	9.2	0.02
10	107	126	1.42	8.9	0.05
10^4	0.06	0.13	1.58	9.7	3.5
d_p (nm)					
80	4550	4784	0.90	2.0	0.005
20 ($\sigma_{p,geo}=2$)	505	–	0.95	3.5	0.01
20	107	126	1.42	8.9	0.05
1	0.03	0.07	2.17	201	6.1

* Taken at the end of the simulation, i.e. when $\overline{N_p}=100$.

decreasing Kn_n in Fig. 3, it corresponds to a general decrease of z, which appears to be more sensitive to the change of agglomeration regime.

For the calculated kinetics exponents, the last two columns of Table 1 report a representative Kn_f and Kn_n. These results are in good agreement with the *ex-situ* analysis of soot coagulation (without surface growth and nucleation) reported in [51] for soot particles in the $0.5 < Kn_f < 10$ flow regimes where $z = 1.4 - 1.9$ was obtained when the agglomeration is in the near-free molecular regime to $z = 0.69 - 0.72$ when agglomeration is in the near-continuum flow regime. Although it is not reported, according to the simulations of coagulation, where better agreement is found based on a transition coagulation kernel, it is concluded that agglomeration takes place in the BLCA-DLCA transition regime. The present results show $z = 1.42$ when $Kn_f \sim 8.9$ and $z = 0.9$ when $Kn_f \sim 2.0$. Additionally, the current results are in qualitatively good agreement with the sensitivity analysis of the population balance equation conducted in [52], where $z = 0.7$ was reported in the transition regime, $z = 1.0$ in the continuum and $z = 2.0$ in the free molecular flow regimes for agglomerates consisting of imposed $D_f = 1.0 - 3.0$. The kinetics of agglomeration is determined by the number of collisions between agglomerates over time. This is quantified by the collision or coagulation kernels to be discussed in the following section.

3.3. Coagulation kernels

As explained in the introduction, an important input parameter for the Population Balance Equation for evaluating the evolution of the particle size distribution is the coagulation kernel ($k(i,j)$, i.e. the rate of collisions between particles consisting of i and j monomers). Fig. 4(a-b) show the dimensionless coagulation kernel H for monodisperse particles as formulated by Thajudeen et al. [53],

$$\mathrm{H} = \frac{k_{ii} m_i \pi^2 \mathrm{R}_{s,ii}}{f_i \mathrm{PA}_{ii}^2}, \tag{1}$$

where k_{ii}, m_i, and f_i are the coagulation kernel, mass and friction coefficient respectively. The symbols in the figure correspond to the k_{ii} obtained from the present simulation based on the local slopes of Fig. 3(a-b) ($k_{ii} = 2dn^{-1}/dt$ as proposed by Heine et al. [42]). Mass and friction coefficients are evaluated from the MCAC simulations. Also, $\mathrm{R}_{s,ii}$ and PA_{ii} are the Smoluchowski radius and projected area, respectively. Both are calculated based on the fractal dimensions reported later in this work (see Fig. 7) and the expressions proposed in [53]. All the above mentioned properties are evaluated based on population average values. In order to compare the current results (symbols) with the empirical relation proposed in [53] (continuous solid curves), the results are plotted as a function

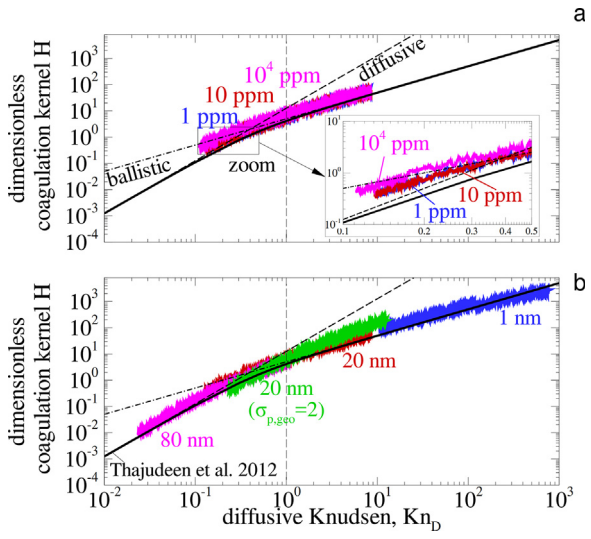

Fig. 4. Dimensionless coagulation kernel H as a function of the diffusive Knudsen number Kn_D for (a) different particle volume fraction and (b) different monomer diameters.

of the diffusive Knudsen number as introduced by the same authors and calculated as follows,

$$Kn_D = \frac{(2 m_i k_B T)^{1/2} \pi \mathrm{R}_{s,ii}}{f_i \mathrm{PA}_{ii}}, \tag{2}$$

where k_B is the Boltzmann constant. This Knudsen number has the same physical meaning as Kn_n used in the present study but it is limited to a diluted system. As can be seen in Fig. 4(a-b) for all the simulated cases, very good agreement is found between the present results and those by Thajudeen et al. [53] even if the considered range of primary particle diameters and volume fraction is huge. Nevertheless, a departure is observed for the high volume fraction case (10^4 ppm, Fig. 4(a)) explained by the deviation from the diluted assumption made in [53]. This illustrates that MCAC is able to reproduce reliable kernels from ballistic to diffusive regimes since Thajudeen et al. [53] obtained their results based on Langevin Dynamics simulations. However, MCAC is able to explore larger volume fractions and also to take into account, the primary particle polydispersity with a reduced computational cost. Also, contrary to Thajudeen et al. [53], the agglomerate morphology is not imposed in MCAC simulations. It is interesting to note in Fig. 4(b), that monomer polydispersity tends to increase the dimensionless coagulation kernels, especially for larger Kn_D.

3.4. Self preserving size distributions

It has been suggested in the literature that agglomerates attain a Self-Preserving Size Distribution (SPSD) in both the free molecular and continuum flow regimes [54,23]. In particular, concerning soot without nucleation and surface growth [51], or simply when coagulation is dominant, SPSD has been experimentally observed [55]. This means that, after a given time, the dimensionless representation of the density of particles having a certain number of primary particles, converges toward an asymptotic form [56]. Under this condition, the coagulation kernel $k(i,j)$ is a self-similar function scaling according to the homogeneity coefficient λ. Thus, λ can be used to monitor the SPSD. Therefore, it is very interesting to study how this parameter is sensitive to a change in agglomeration or flow regimes. Usually, λ is determined by fitting the SPSD [7,3] or, as proposed by Dongen and Ernst [57], relying on the scaling hypothesis ($\lambda = 1 - 1/z$) based on the above mentioned kinetic exponent z. However, these approaches may be inaccurate and non robust. For these reasons, an original and more robust method for determining λ and thus the agglomerate size distribution is proposed here. Indeed, the SPSD is found to follow a generalized Gamma distribution function (the demonstration is given in A),

$$f(x) = \frac{(p/a^d)}{\tilde{x}\,\Gamma(d/p)} X^{d-1} \exp\left[-\left(\frac{X}{a}\right)^p\right], \tag{3}$$

where $f(x)$ is the probability density function of the particle size. Here, x corresponds to one of the four size parameters considered in the present study as indicated in Table 2. In this equation, $\Gamma(y) = \int_0^\infty t^{y-1}e^{-t}\,dt$ is the Gamma function, p is a dimension parameter, $a = (1-\lambda)^{-1/p}, d = p(1-\lambda)$, and $X = x/\tilde{x}$ is a dimensionless size where $\tilde{x} = \left(\overline{x^p}\right)^{1/p}$. In addition to this generalized analytical expression for the SPSD, an analytical expression of the q-moment of the generalized SPSD is provided in B. In Eq. (4), in particular, the q-moment based on the volume equivalent diameter $d_v = (6v/\pi)^{1/3}$ distribution is shown,

$$\overline{d_v^q} = \tilde{d_v}^{\,q} \frac{\Gamma(1-\lambda+q/3)}{(1-\lambda)^{q/3}\Gamma(1-\lambda)}, \tag{4}$$

In the present work, the evaluation of the homogeneity coefficient λ based on a new and robust method is proposed. It consists in solving Eq. (4) based on the volume equivalent diameters distribution by letting the homogeneity coefficient as the unknown searched variable. This operation is performed for the first ($q = 1$) and second ($q = 2$) moments of the distribution, thus providing two corresponding homogeneity coefficients denoted as λ_{M1} and λ_{M2}, respectively and reported in Fig. 5 with filled and empty symbols, respectively.

Let's begin the analysis by focusing on the monodisperse case. At short times (corresponding to small $\overline{N_p}$), both, λ_{M1} and λ_{M2} are different, indicating the initial size distributions (Dirac) are not self-preserving. That difference is not clear in Fig. 5 due to the amplitude of the overall variations of these parameters. Nevertheless, a study of the difference between λ_{M1} and λ_{M2} (see Fig. S1 in the supporting material) enables determining the time (or equivalently the mean N_p) needed to reach a convergence, i.e. the time needed to tend toward a self-preserving state. This time-lag for SPSD is found to be on average $\sim 5\tau_a$ (not shown here) and appears to be equivalent to $\overline{N_p} \approx 20$ as represented by the gray zone in this figure. Consequently, before this convergence, the corresponding value of the homogeneity coefficient ($-\infty$ in the present case) is difficult to interpret in physical terms even considering the initial value is clearly determined by the monodisperse agglomerate size distribution. However, for longer times (or larger $\overline{N_p}$), both parameters generally converge well toward a common value evolving in time suggesting that the particle size distributions are quasi self-preserving throughout the agglomeration process. The range of observed values of λ for larger agglomerates is between -0.5 and 0.5, in the acceptable physical range discussed by Pierce et al. [3], and in good agreement with experimentally measured ones. Indeed, Wang and Sorensen [9] reported λ between -0.28 and -0.46 in the range of $Kn_f \approx 1.8 - 2.2$ for silica and titania nanoparticles. From the results of Maricq [51], λ between -0.39 and -0.45 are deduced (based on the scaling approach) for soot particles in the same range of fluid Knudsen numbers.

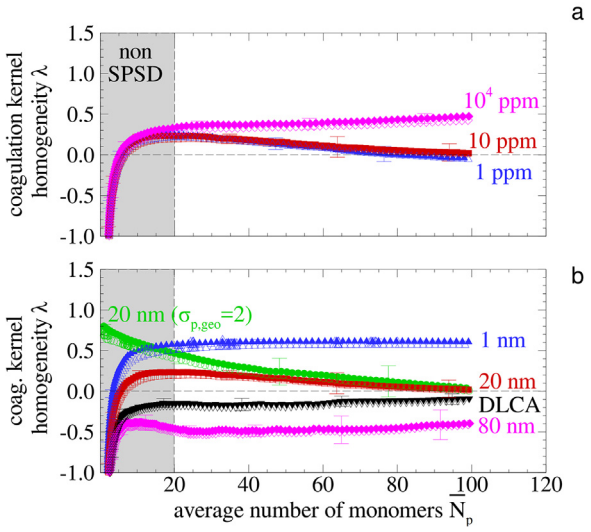

Fig. 5. Coagulation kernel homogeneity coefficients for (a) different particle volume fraction and (b) different monomer diameters. Calculated from the first (λ_{M1}, filled symbols) and second (λ_{M2}, non-filled symbols) moments of the volume equivalent diameter distributions.

The largest values of λ are observed for $d_p = 1$ nm and $f_v = 10^4$ ppm, where the agglomeration is ballistically limited (see Fig. 2). In this regime, the increase in particle sizes means an increase in the coagulation kernels since the projected particle area increases faster than the drag force [21] therefore, positive λ are expected. In the case of $d_p = 80$ nm, corresponding to agglomeration in the DLCA-near diffusive flow regime ($Kn_f \sim 2.0$), negative values of λ are observed, meaning that larger agglomerates have smaller coagulation kernels as a consequence of the increase in the drag force due to lower Cunningham correction factors and the number of monomers per agglomerate [37].

To evaluate the impact of the flow regime, the case of $d_p = 80$ nm and $f_v = 10$ ppm, for which $\lambda = -0.5$ (pink symbols), is again simulated by forcing the drag force to stay in the "classical" DLCA-Epstein regime throughout the agglomeration process to serve as a reference case (black symbols, labeled DLCA in the figure). Note that the reference DLCA case is much more stable in terms of λ compared to the initial simulations for which flow regime variation is taken into account. Also, an asymptotic and dif-

Table 2
Parameters for the generalized SPSD given by Eq. (3).

Size descriptor	x	p
Number monomers	N_p	1
Volume eq. diameter	d_v	3
Gyration diameter*	d_g	D_f
Mobility diameter**	d_m	D_{fm}

* Gyration diameter based or mass fractal dimension D_f.
** Mobility diameter based fractal dimension D_{fm} (scaling exponent).

ferent value is quickly attained. This highlights the importance of considering the natural evolution of the flow regime. This is confirmed by the observed important role played by d_p as shown in Fig. 5(b), which is a key parameter for evaluating the friction coefficient and its dependence on the fluid regime. In comparison, f_v seems to have a less relative impact.

Let's now focus on the case of polydisperse monomers represented by green circles symbols in Fig. 5(b). For short times (corresponding to small $\overline{N_p}$), both, λ_{M1} and λ_{M2} do not differ considerably. This is explained by the fact that SPSD is not very different from a lognormal distribution [58,59]. Also, a very different behaviour for λ_{M1} and λ_{M2} can be noted in this case compared to monodisperse monomers. This is a promising result suggesting that an experimental tracking of the evolution of the homogeneity coefficient at early stages of the agglomeration process, could be used to assess the primary particle polydispersity.

As can be noted, the convergence between λ_{M1} and λ_{M2} is reached for a larger agglomerate size ($\overline{N_p} \sim 70$) when primary particle polydispersity is relevant. But when comparing the polydisperse and monodisperse cases (with the same monomers geometric mean), a convergence toward the same asymptotic value is observed, suggesting that primary particle polydispersity does not influence the agglomeration process at long times. This is consistent with the results of Friedlander [48] and Goudeli et al. [60].

Since homogeneity coefficients are found to be more influenced by the monomer diameters than particle volume fraction, Fig. 6(a–c) reports the corresponding asymptotic SPSD obtained as a function of the dimensionless volume equivalent diameter, gyration and mobility diameters, respectively. To avoid overloading the figure, direct evaluation of the size distribution is reported in symbols only for the reference case (i.e. $d_p = 20$ nm), whereas continuous curves correspond to the theoretical self-preserving functions (Eq. 3) evaluated with the final λ_{M1} found in Fig. 5, i.e. when $\overline{N_p} = 100$. First of all, a good agreement with the theoretical expression for the reference case is observed. This confirms that the size distribution corresponds well to a SPSD. Secondly, the smaller the primary particle diameter, the wider the distribution becomes. This is also found with larger f_v (not presented here) indicating that ballistic and free molecular flow regimes are characterized by wider agglomerate size distributions. This result is in agreement with coalescing spheres for all regimes [54] and with agglomerates in the asymptotic regimes [23]. It is worth highlighting the ability of MCAC to simulate the quasi-SPSD in the transition regime in terms of the different agglomerate size parameters (volume equivalent, gyration, and mobility radius). However, the size distribution expressed in terms of mobility diameter, does not converge exactly towards a lognormal size distribution (dashed red line in Fig. 6(c)) as experimental measurements usually report. This discrepancy may be related to some physical phenomena, relevant for soot formation in flames, not considered in the present Monte Carlo approach (for example, interaction potentials, surface growth or thermophoretic forces). It should also be noted that the simulated agglomerates are simplified in terms of morphology (one point contact spheres) compared to real soot particles as experimentally seen in TEM images [46,61].

The comparison of the particle size distribution, as expressed in terms of d_v, d_m or d_g show different degrees of apparent polydispersity. Indeed, for current simulations of $f_v = 10$ ppm and $d_p = 1$–20 nm, the following geometric standard deviations are obtained $\sigma_{geo,dv} = 1.50$–$1.85, \sigma_{geo,dm} = 1.58$–$1.98$ and $\sigma_{geo,dg} = 1.95$–2.60 (these results are reported in Fig. S2 in the supporting material). It is interesting to observe the good agreement with the ranges of polydispersities observed experimentally. In fact, for soot particles in ethylene diffusion flames, it has been reported that $\sigma_{geo,dm} = 1.31$–1.33 as measured by Differential Mobility Spectrometer [62] and $\sigma_{geo,dg} = 2.1$ and ≈ 2.1–2.9 based on TEM images analysis reported in [62,46], respectively.

3.5. Agglomerate morphology

The morphology of agglomerates is described by the population based fractal dimension D_f and prefactor k_f obtained based on the fractal law,

$$\frac{v_a}{\overline{v_p}} = k_f \left(\frac{d_g}{\overline{d_p}} \right)^{D_f} \tag{5}$$

where $v_a/\overline{v_p}$ is the ratio between the agglomerate volume and the average monomers volume (corresponding to the number of primary particles N_p), d_g is the diameter of gyration and $\overline{d_p}$ is defined here as the numerical average monomer diameter. It should be noted that there is no strict rule for using the fractal law when dealing with polydisperse primary particles [63,64]. Defining the representative primary particle radius differently affects the thus determined fractal prefactor but not the fractal dimension. Also, the fractal law has been considered to be valid only for sufficiently large agglomerates (typically $\overline{N_p} > 20$). When plotting N_p in a log-log plot as a function of $d_g/\overline{d_p}$, a linear fit easily provides D_f and k_f. This procedure is repeated in the present study at each time iter-

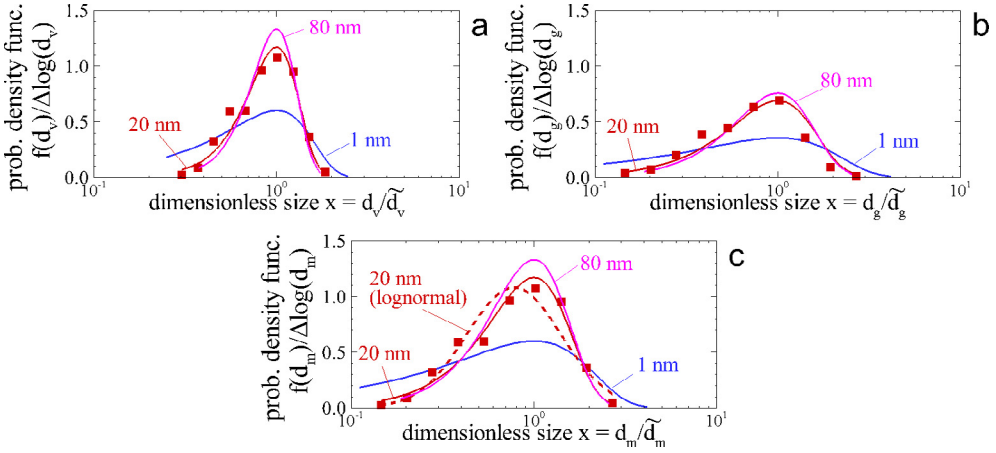

Fig. 6. Asymptotic particle size distribution expressed in terms of (a) the volume equivalent diameter, (b) the diameter of gyration and (c) the mobility diameter.

ation during the agglomeration process. The resulting fractal dimensions D_f are reported in Fig. 7(a-b) as a function of the mean number of primary particles per agglomerate. An exactly time-invariant fractal dimension is not achieved. However, its variation is very small for $\overline{N_p} > 20$ and depending on the application it may be neglected. This is in agreement with the results obtained in [19,65] which indicated a non-fractal domain for $\overline{N_p} < 20$, indicated in gray in the figure. It should be noted that this limit is qualitative and values between 15 to 30 can be found in the literature [66,67]. In Fig. 7(a), an increase in the approximately asymptotic fractal dimension as a function of particle volume fraction is observed, thus being in agreement with previous studies [43,68,25,19]. This is because agglomeration becomes more ballistic. Nevertheless, for soot agglomeration processes, such high volume fractions may not be common. Furthermore, the observed variation of D_f is not large (between 1.80 and 1.88). Thus, it is unlikely that this parameter alone can explain the variability of the fractal dimensions found in the literature [46]. Fig. 7(b) shows the more influencing effect of the primary particle diameter (D_f between 1.62 and 1.86). First, it is very remarkable that this value decreases when increasing the monomer diameters. The present results seems to indicate that the primary particle diameter, that plays an important role in the evaluation of the drag force (see Eq. (2) in the preceding work [4]) and therefore, due to the change in flow regime, has a significant impact on soot morphology. Thus, a small fractal dimension (down to 1.62) can result in the agglomeration of large monodisperse primary particles or at least containing a few large primary particles as seen in Fig. 7(b) for the polydisperse case $\sigma_{p,geo} = 2$ reported in green. Some authors [60,69] also reported consistent dependencies of particle morphology on primary particle polydispersity, however the simultaneous change in agglomeration and flow regimes was not taken into account.

As discussed before, the change in flow regime is evaluated by comparing the results with the reference DLCA-Epstein case (black inverted triangle symbols in Fig. 7(b)). In this case, an asymptotic fractal dimension of 1.77 is found. Therefore, taking into account the change in the flow regime, may have a strong impact in the agglomerate morphology.

The evolution of k_f as a function of $\overline{N_p}$ can be interpreted as a morphological signature different from the fractal dimension [71]. Nevertheless, as for the fractal dimension, the fractal prefactor is more influenced by the primary particle diameter and polydispersity than by the particle volume fraction (see Fig. S3 in the supporting material). An interesting variation is observed when analyzing the fractal prefactor as a function of the corresponding fractal dimension. This is shown in Fig. 7(c-d) for $\overline{N_p} > 20$. The results are compared with the literature [66,70]. The overall trend is that both parameters are inversely related, which is in accordance with the cited references. It is interesting to note that for both $d_p = 80$ nm ($\sigma_{p,geo} = 1$) and $d_p = 20$ nm ($\sigma_{p,geo} = 2$), the relative variation observed during the agglomeration process shows a very different D_f compared with other simulated cases.

Finally, when analyzing the fractal dimension in Fig. 7(b) at large $\overline{N_p}$, a significant sensitivity to the primary particle diameter is observed. Thus, the analysis is extended up to d_p = 160 nm to explore this dependency. The results are presented in Fig. 8 where, the fractal dimensions of agglomerates simulated by MCAC, are compared with the experimental measurements reported by [72] and the classical DLCA and BLCA limits under fixed flow regimes [17]. Here, the role played by primary particle size on agglomerate

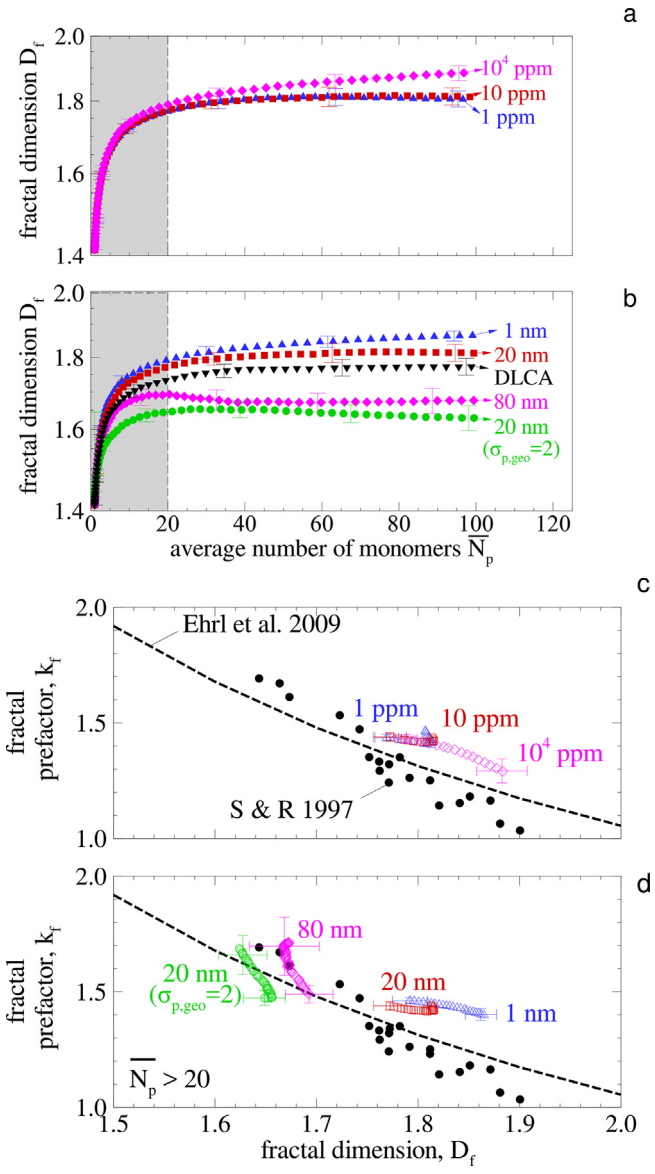

Fig. 7. (a-b) Population based fractal dimension D_f as a function of the average number of monomers per agglomerate $\overline{N_p}$. (c-d) Fractal prefactor dependence on the fractal dimension for $\overline{N_p} > 20$ compared with Ehrl et al. [66] and Sorensen & Roberts [70].

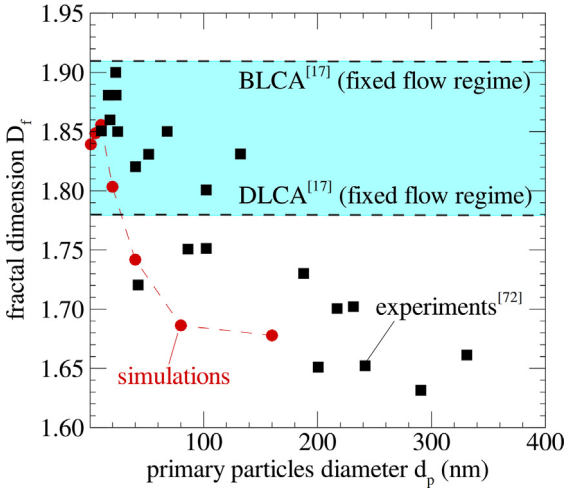

Fig. 8. The variation of the fractal dimension as a function of the primary particle diameter compared with the BLCA ($D_f = 1.91$) and DLCA ($D_f = 1.78$) limits under fixed flow regimes [17] and experimental measurements [72].

morphology becomes evident as smaller fractal dimensions are found for larger d_p, being in good agreement with the referenced experimental data [72]. It is very remarkable that fractal dimensions below the classical DLCA limit are observed when taking into account the simultaneous change of agglomeration and flow regimes.

4. Conclusions

Numerical simulations of soot agglomeration are carried out based on the recently published Monte Carlo Aggregation Code, MCAC, taking into account the variation through time of the nearest-neighbor and fluid Knudsen numbers. This enables a continuous transition to occur from ballistic to diffusive agglomeration and, simultaneously, a continuous transition from free molecular to near-continuum flow regimes. Remarkably, considering that the change in both regimes is seldom found in the literature, excepting the notable work of Thajudeen et al. [24], focused on the determination of the agglomerates projected area and hydrodynamic radius, under diluted conditions (low particle volume fraction). This work is extended here to study the agglomeration kinetic, size distribution and morphology. The present work explores the role played by the particle volume fraction, the primary particle size and polydispersity.

Except in the case of $f_v = 10^4$ ppm, the dimensionless coagulation kernel is found to be in good agreement with Thajudeen et al. [53]. The latter also found good agreement with subsequent works [73,74,44], therefore it is recommended for conducting population balance simulations of nanoparticle coagulation under diluted systems [19,75,76]. This is especially important for nanoparticle coagulation in the transition regime where collision kernels are treated separately and a limit to the fractal dimension is usually considered for BLCA [51,52].

The current investigation also enables some very interesting and original results to be highlighted. In particular, the role played by the primary particle size and polydispersity. Indeed, it is observed that increasing the primary particle diameter:

- Slows down the agglomeration kinetics. Increases the agglomerate size geometric standard deviation while keeping the quasi self-preserving size distribution.
- Induces an substantial decrease in the mass fractal dimension down to $D_f = 1.67$ for large monomers ($d_p = 80$ nm) at flame conditions. This is much lower than the typical 1.78 usually considered for agglomerates generated by pure DLCA. This was empirically observed by Wu et al. [72,19] who highlighted the lack of explanation for this trend.

An inverse correlation between the fractal dimension and prefactor is observed during the agglomeration process. This has only been studied previously in an asymptotic fashion [66,70]. This finding is of great importance for improving the physical representation of agglomerates generated with tunable algorithms [64,77]. The homogeneity coefficient is found to be (highly) dependent on the primary particle polydispersity only at the beginning of the agglomeration process.

All these results highlight how the change of regimes experienced by the particles has a significant impact on the dynamics of agglomeration, particle size distribution and morphology. In addition, the present work proposes:

- A generalized expression for the Self Preserving Size Distribution taking the form of a generalized Gamma distribution irrespective of the considered agglomerate size parameter. This opens the way to an experimental determination of the homogeneity coefficient by measuring the distribution of gyration diameters by light-scattering [9,45,62,78,79], by TEM images analysis [46] or electrical mobility particle classification [37,51]. It also enables the different ranges of agglomerate size polydispersity to be understood when determined as a function of the selected size parameter (the standard deviation is found to be larger for gyration diameters than for mobility or equivalent volume ones).
- A new and robust method for numerically determining the coagulation homogeneity coefficient λ, is introduced, being therefore, an alternative to the classical scaling approach [57,34,33]. It is based on the first and second moments of the introduced generalized self-preserving particle size distribution [3,22,7].

Future developments of MCAC will focus on the role played by surface growth occurring during the agglomeration process. Other physical effects could be considered, such as interaction potentials [19,80] or thermophoretic forces [81]. Additionally, understanding the transition towards crowded systems and possibly the formation of gels [45,34,33] could be done, possibly focusing on the BLCA-continuum transition regime, which has not been systematically studied. Finally, MCAC may be able to address the simulation of super agglomerates formation [82]. MCAC has been implemented in c++, and it is publicly available in the following link https://gitlab.coria-cfd.fr/MCAC/MCAC.

CRediT authorship contribution statement

J. Morán: Conceptualization, Validation, Formal analysis, Writing - original draft, Visualization. **J. Yon:** Conceptualization, Software, Writing - review & editing, Supervision, Project administration, Funding acquisition. **A. Poux:** Conceptualization, Software, Formal analysis, Validation, Writing - review & editing. **F. Corbin:** Software, Formal analysis. **F.-X. Ouf:** Conceptualization, Writing - review & editing. **A. Siméon:** Conceptualization, Formal analysis, Writing - review & editing.

Declaration of Competing Interest

The authors declare that they have no known competing financial interests or personal relationships that could have appeared to influence the work reported in this paper.

Acknowledgments

This work is financed by ANR ASTORIA (N° ANR-18-CE05-0015) and the Region of Normandy (project RIN Gaspropres). The authors also thank the CRIANN numerical resources supported by the Normandy region. Thanks are also due to Francisco Cepeda and James Brian Mitchell for their re-reading of the manuscript.

Appendix A. The generalized self preserving size distribution

Oh and Sorensen [7] introduced the following Self-preserving particles size distribution as expressed in terms of the volume of aggregates,

$$n(v) = M_1 s_b^{-2} \phi(x), x = v/s_b \tag{A.1}$$

where $n(v)dv$ represents the number density of particles whose volume is between v and $v + dv$, and where $s_b = M_b/M_{b-1}$, considering M_b as the b-moment of the volume-based particle size distribution,

$$M_b = \int_0^\infty v^b n(v) dv \tag{A.2}$$

Additionally, $\phi(x)$ corresponds to the time-invariant shape of the SPSD,

$$\phi(X) = AX^{-\lambda}\exp\left[-(b-\lambda)X\right], \tag{A.3}$$

where $A = (b-\lambda)^{b-\lambda}/\Gamma(b-\lambda)$. Therefore, they finally arrive at the following expression by rewriting Eq. (A.1) considering $b = 1$,

$$n(v) = \frac{1}{v}\frac{(1-\lambda)^{1-\lambda}}{\Gamma(1-\lambda)}X^{1-\lambda}\exp\left[-(1-\lambda)X\right], X = v/\overline{v} \tag{A.4}$$

This expression can be converted to a probability density function $f(v)$ by calculating,

$$f(v)dv = \frac{n(v)dv}{\int_0^\infty n(v)dv} \tag{A.5}$$

$$f(v) = \frac{1}{\overline{v}}\frac{(1-\lambda)^{1-\lambda}}{\Gamma(1-\lambda)}X^{-\lambda}\exp\left[-(1-\lambda)X\right], X = v/\overline{v} \tag{A.6}$$

For any equivalent diameter x related to the volume of the aggregate according to the following expression,

$$v = \alpha x^p \tag{A.7}$$

where α and p correspond to a prefactor and exponent, respectively. Now, considering the probability of finding a particle with a volume between v and $v + dv$ is the same as the probability of finding a particle with an equivalent diameter between x and $x + dx$, i.e. $f(v)dv = f(x)dx$ therefore,

$$f(x) = f(v)\alpha p x^{p-1},\ v = \alpha x^p \tag{A.8}$$

Based on Eq. (A.6) and introducing $\widetilde{x} = \left(\overline{x^p}\right)^{1/p}$,

$$f(x) = \frac{p}{\widetilde{x}}\frac{(1-\lambda)^{1-\lambda}}{\Gamma(1-\lambda)}X^{p(1-\lambda)-1}\exp\left[-(1-\lambda)X^p\right], X = x/\widetilde{x} \tag{A.9}$$

Note that Eq. (A.9) is independent of the prefactor α. Finally, by introducing the following parameters $a = (1-\lambda)^{-1/p}$ and $d = p(1-\lambda)$, it is shown that Eq. (A.9) corresponds to a generalized Gamma distribution,

$$f(x) = \frac{(p/a^d)}{\widetilde{x}\,\Gamma(d/p)}X^{d-1}\exp\left[-\left(\frac{X}{a}\right)^p\right], X = x/\widetilde{x} \tag{A.10}$$

Appendix B. q-moment of the generalized SPSD

The moment of order q of a distribution of a general probability density function $f(x)$ is,

$$\overline{x^q} = \int_0^\infty x^q f(x)dx, \tag{B.1}$$

considering the $f(x)$ given by Eq. (A.10) the following expression is obtained,

$$\overline{x^q} = \widetilde{x}^q a^q \frac{\Gamma\left(\frac{a+p}{q}\right)}{\Gamma(d/p)}, \tag{B.2}$$

by replacing the previously defined parameters a and d,

$$\overline{x^q} = \widetilde{x}^q \frac{\Gamma(1-\lambda+p/q)}{(1-\lambda)^{q/p}\Gamma(1-\lambda)} \tag{B.3}$$

Appendix C. Supplementary material

Supplementary data associated with this article can be found, in the online version, at https://doi.org/10.1016/j.jcis.2020.04.085.

References

[1] G. Nichols, S. Byard, M.J. Bloxham, J. Botterill, N.J. Dawson, A. Dennis, V. Diart, N.C. North, J.D. Sherwood, A review of the terms agglomerate and aggregate with a recommendation for nomenclature used in powder and particle characterization, J. Pharm. Sci. 91 (10) (2002) 2103–2109, https://doi.org/10.1002/jps.10191.

[2] C. Sorensen, The mobility of fractal aggregates: a review, Aerosol Sci. Technol. 45 (7) (2011) 765–779, https://doi.org/10.1080/02786826.2011.560909.

[3] F. Pierce, C. Sorensen, A. Chakrabarti, Computer simulation of diffusion-limited cluster-cluster aggregation with an epstein drag force, Phys. Rev. E 74 (2) (2006) 021411, https://doi.org/10.1103/PhysRevE.74.021411.

[4] J. Morán, J. Yon, A. Poux, Monte carlo aggregation code (mcac) part 1: Fundamentals, J. Colloid Interface Sci. 569 (2020) 184–194, https://doi.org/10.1016/j.jcis.2020.02.039.

[5] R. Puri, T. Richardson, R. Santoro, R. Dobbins, Aerosol dynamic processes of soot aggregates in a laminar ethene diffusion flame, Combust. Flame 92 (3) (1993) 320–333, https://doi.org/10.1016/0010-2180(93)90043-3.

[6] C. Feldermann, H. Jander, H.G. Wagner, Soot particle coagulation in premixed ethylene/air flames at 10 bar, Zeitschrift für Physikalische Chemie 186 (2) (1994) 127–140, https://doi.org/10.1524/zpch.1994.186.Part_2.127.

[7] C. Oh, C. Sorensen, Light scattering study of fractal cluster aggregation near the free molecular regime, J. Aerosol Sci. 28 (6) (1997) 937–957, https://doi.org/10.1016/S0021-8502(96)00488-0.

[8] A. Kazakov, M. Frenklach, Dynamic modeling of soot particle coagulation and aggregation: Implementation with the method of moments and application to high-pressure laminar premixed flames, Combust Flame 114 (3–4) (1998) 484–501, https://doi.org/10.1016/S0010-2180(97)00322-2.

[9] G. Wang, C. Sorensen, Aggregation kernel homogeneity for fractal aggregate aerosols in the slip regime, Aerosol Sci. Technol. 34 (3) (2001) 297–306, https://doi.org/10.1080/02786820118313.

[10] D. Kim, S. Park, Y. Song, D. Kim, K. Lee, Brownian coagulation of polydisperse aerosols in the transition regime, J. Aerosol Sci. 34 (7) (2003) 859–868, https://doi.org/10.1016/S0021-8502(03)00055-7.

[11] D. Kim, S. Hong, Y. Kim, K. Lee, Deposition and coagulation of polydisperse nanoparticles by brownian motion and turbulence, J. Aerosol Sci. 37 (12) (2006) 1781–1787, https://doi.org/10.1016/j.jaerosci.2006.07.001.

[12] P.E. Wagner, M. Kerker, Brownian coagulation of aerosols in rarefied gases, J. Chem. Phys. 66 (2) (1977) 638–646, https://doi.org/10.1063/1.433937.

[13] C. Davies, Coagulation of aerosols by brownian motion, J. Aerosol Sci. 10 (2) (1979) 151–161, https://doi.org/10.1016/0021-8502(79)90064-8.

[14] K. Lee, H. Chen, Coagulation rate of polydisperse particles, Aerosol Sci. Technol. 3 (3) (1984) 327–334, https://doi.org/10.1080/02786828408959020.

[15] G. Narsimhan, E. Ruckenstein, The brownian coagulation of aerosols over the entire range of knudsen numbers: Connection between the sticking probability and the interaction forces, J. Colloid Interface Sci. 104 (2) (1985) 344–369, https://doi.org/10.1016/0021-9797(85)90044-X.

[16] D.D. Huang, J.H. Seinfeld, W.H. Marlow, Bgk equation solution of coagulation for large knudsen number aerosols with a singular attractive contact potential, J. Colloid Interface Sci. 140 (1) (1990) 258–276, https://doi.org/10.1016/0021-9797(90)90341-K.

[17] P. Meakin, A historical introduction to computer models for fractal aggregates, J. Sol-Gel. Sci. Technol. 15 (2) (1999) 97–117, https://doi.org/10.1023/A:1008731904082.

[18] S. Lazzari, M. Lattuada, Growth and aggregation regulate clusters structural properties and gel time, J. Phys. Chem. B 121 (11) (2017) 2511–2524, https://doi.org/10.1021/acs.jpcb.6b12682.

[19] S. Lazzari, L. Nicoud, B. Jaquet, M. Lattuada, M. Morbidelli, Fractal-like structures in colloid science, Adv. Colloid Interface Sci. 235 (2016) 1–13, https://doi.org/10.1016/j.cis.2016.05.002.

[20] A.Y. Kim, J.C. Berg, Fractal aggregation: scaling of fractal dimension with stability ratio, Langmuir 16 (5) (2000) 2101–2104, https://doi.org/10.1021/la990841n.

[21] R.D. Mountain, G.W. Mulholland, H. Baum, Simulation of aerosol agglomeration in the free molecular and continuum flow regimes, J. Colloid Interface Sci. 114 (1) (1986) 67–81, https://doi.org/10.1016/0021-9797(86)90241-9.

[22] W.R. Heinson, F. Pierce, C.M. Sorensen, A. Chakrabarti, Crossover from ballistic to epstein diffusion in the free-molecular regime, Aerosol Sci. Technol. 48 (7) (2014) 738–746, https://doi.org/10.1080/02786826.2014.922677.

[23] E. Goudeli, M.L. Eggersdorfer, S.E. Pratsinis, Coagulation–agglomeration of fractal-like particles: structure and self-preserving size distribution, Langmuir 31 (4) (2015) 1320–1327, https://doi.org/10.1021/la504296z.

[24] T. Thajudeen, S. Deshmukh, C.J. Hogan Jr, Langevin simulation of aggregate formation in the transition regime, Aerosol Sci. Technol. 49 (2) (2015) 115–125, https://doi.org/10.1080/02786826.2015.1008971.

[25] R. Zahaf, S.-K. Kim, J. Shin, K. Park, T.-Y. Choi, D. Lee, Effect of volume fraction on transient structural behavior of aerosol particles using off-lattice kinetic monte carlo simulation, Aerosol Sci. Technol. 49 (12) (2015) 1242–1255, https://doi.org/10.1080/02786826.2015.1116681.

[26] C. Betrancourt, F. Liu, P. Desgroux, X. Mercier, A. Faccinetto, M. Salamanca, L. Ruwe, K. Kohse-Höinghaus, D. Emmrich, A. Beyer, et al., Investigation of the size of the incandescent incipient soot particles in premixed sooting and nucleation flames of n-butane using lii, him, and 1 nm-smps, Aerosol Sci.

Technol. 51 (8) (2017) 916–935, https://doi.org/10.1080/02786826.2017.1325440.
[27] F. Schulz, M. Commodo, K. Kaiser, G. De Falco, P. Minutolo, G. Meyer, D. Andrea, L. Gross, Insights into incipient soot formation by atomic force microscopy, Proc. Combust. Inst. 37 (1) (2019) 885–892, https://doi.org/10.1016/j.proci.2018.06.100.
[28] F. Patiño, J. Cruz, I. Verdugo, J. Morán, J. Consalvi, F. Liu, X. Du, A. Fuentes, Soot primary particle sizing in a n-heptane doped methane/air laminar coflow diffusion flame by planar two-color tire-lii and tem image analysis, Fuel 266 (2020) 117030, https://doi.org/10.1016/j.fuel.2020.117030.
[29] M.L. Botero, N. Eaves, J.A. Dreyer, Y. Sheng, J. Akroyd, W. Yang, M. Kraft, Experimental and numerical study of the evolution of soot primary particles in a diffusion flame, Proc. Combust. Inst. 37 (2) (2019) 2047–2055. doi: https://doi.org/10.1016/j.proci.2018.06.185.
[30] N.A. Eaves, Q. Zhang, F. Liu, H. Guo, S.B. Dworkin, M.J. Thomson, Coflame: A refined and validated numerical algorithm for modeling sooting laminar coflow diffusion flames, Comput. Phys. Commun. 207 (2016) 464–477, https://doi.org/10.1016/j.cpc.2016.06.016.
[31] A. Jerez, J.-L. Consalvi, A. Fuentes, F. Liu, R. Demarco, Soot production modeling in a laminar coflow ethylene diffusion flame at different oxygen indices using a pah-based sectional model, Fuel 231 (2018) 404–416, https://doi.org/10.1016/j.fuel.2018.05.103.
[32] S. Friedlander, C. Wang, The self-preserving particle size distribution for coagulation by brownian motion, J. Colloid interface Sci. 22 (2) (1966) 126–132, https://doi.org/10.1016/0021-9797(66)90073-7.
[33] P. Liu, W.R. Heinson, C.M. Sorensen, R.K. Chakrabarty, Kinetics of sol-to-gel transition in irreversible particulate systems, J. Colloid Interface Sci. 550 (2019) 57–63, https://doi.org/10.1016/j.jcis.2019.04.067.
[34] R.H. Ebini, C.M. Sorensen, Light scattering studies of the sol-to-gel transition in particulate systems, J. Colloid Interface Sci. 556 (2019) 577–583, https://doi.org/10.1016/j.jcis.2019.08.075.
[35] F. Leyvraz, Scaling theory and exactly solved models in the kinetics of irreversible aggregation, Phys. Rep. 383 (2–3) (2003) 95–212, https://doi.org/10.1016/S0370-1573(03)00241-2.
[36] S. di Stasio, A.G. Konstandopoulos, M. Kostoglou, Cluster–cluster aggregation kinetics and primary particle growth of soot nanoparticles in flame by light scattering and numerical simulations, J. Colloid Interface Sci. 247 (1) (2002) 33–46, https://doi.org/10.1006/jcis.2001.8095.
[37] J. Yon, A. Bescond, F.-X. Ouf, A simple semi-empirical model for effective density measurements of fractal aggregates, J. Aerosol Sci. 87 (2015) 28–37, https://doi.org/10.1016/j.jaerosci.2015.05.003.
[38] K. Liffman, A direct simulation monte-carlo method for cluster coagulation, J. Comput. Phys. 100 (1) (1992) 116–127, https://doi.org/10.1016/0021-9991(92)90314-O.
[39] M. Smith, T. Matsoukas, Constant-number monte carlo simulation of population balances, Chem. Eng. Sci. 53 (9) (1998) 1777–1786, https://doi.org/10.1016/S0009-2509(98)00045-1.
[40] F.-X. Ouf, S. Bourrous, S. Fauvel, A. Kort, L. Lintis, J. Nuvoli, J. Yon, True density of combustion emitted particles: a comparison of results highlighting the influence of the organic contents, J. Aerosol Sci. 134 (2019) 1–13, https://doi.org/10.1016/j.jaerosci.2019.04.007.
[41] Y. Wang, S.H. Chung, Soot formation in laminar counterflow flames, Prog. Energy Combust. Sci. 74 (2019) 152–238, https://doi.org/10.1016/j.pecs.2019.05.003.
[42] M. Heine, S.E. Pratsinis, Brownian coagulation at high concentration, Langmuir 23 (19) (2007) 9882–9890, https://doi.org/10.1021/la7012599.
[43] A.E. Gonzalez, M. Lach-Hab, E. Blaisten-Barojas, On the concentration dependence of the cluster fractal dimension in colloidal aggregation, J. Sol-gel Sci. Technol. 15 (2) (1999) 119–127, https://doi.org/10.1023/A:1008783320920.
[44] M. Yu, J. Lin, M. Seipenbusch, J. Cao, Verification of size-resolved population balance modeling for engineered nanoparticles under high concentration, Chem. Eng. J. 323 (2017) 592–604, https://doi.org/10.1016/j.cej.2017.04.128.
[45] P. Sandkühler, J. Sefcik, M. Morbidelli, Kinetics of aggregation and gel formation in concentrated polystyrene colloids, J. Phys. Chem. B 108 (52) (2004) 20105–20121, https://doi.org/10.1021/jp046468w.
[46] D. Cortés, J. Morán, F. Liu, F. Escudero, J.-L. Consalvi, A. Fuentes, Effect of fuels and oxygen indices on the morphology of soot generated in laminar coflow diffusion flames, Energy Fuels 32 (11) (2018) 11802–11813, https://doi.org/10.1021/acs.energyfuels.8b01301.
[47] C. Gu, H. Lin, J. Camacho, B. Lin, C. Shao, R. Li, H. Gu, B. Guan, Z. Huang, H. Wang, Particle size distribution of nascent soot in lightly and heavily sooting premixed ethylene flames, Combust. Flame 165 (2016) 177–187, https://doi.org/10.1016/j.combustflame.2015.12.002.
[48] S.K. Friedlander et al., Smoke, Dust, and Haze, vol. 198, Oxford University Press, New York, 2000.
[49] E. Otto, H. Fissan, S. Park, K. Lee, The log-normal size distribution theory of brownian aerosol coagulation for the entire particle size range: part ii-analytical solution using dahneke's coagulation kernel, J. Aerosol Sci. 30 (1) (1999) 17–34, https://doi.org/10.1016/S0021-8502(98)00038-X.
[50] M. Veshchunov, V. Tarasov, Extension of the smoluchowski theory to transitions from dilute to dense regime of brownian coagulation: triple collisions, Aerosol Sci. Technol. 48 (8) (2014) 813–821, https://doi.org/10.1080/02786826.2014.931567.
[51] M.M. Maricq, Coagulation dynamics of fractal-like soot aggregates, J. Aerosol Sci. 38 (2) (2007) 141–156, https://doi.org/10.1016/j.jaerosci.2006.11.004.
[52] S.N. Rogak, R.C. Flagan, Coagulation of aerosol agglomerates in the transition regime, J. Colloid Interface Sci. 151 (1) (1992) 203–224, https://doi.org/10.1016/0021-9797(92)90252-H.
[53] T. Thajudeen, R. Gopalakrishnan, C.J. Hogan Jr, The collision rate of nonspherical particles and aggregates for all diffusive knudsen numbers, Aerosol Sci. Technol. 46 (11) (2012) 1174–1186, https://doi.org/10.1080/02786826.2012.701353.
[54] M.L. Eggersdorfer, S.E. Pratsinis, Agglomerates and aggregates of nanoparticles made in the gas phase, Adv. Powder Technol. 25 (1) (2014) 71–90, https://doi.org/10.1016/j.apt.2013.10.010.
[55] M.M. Maricq, Physical and chemical comparison of soot in hydrocarbon and biodiesel fuel diffusion flames: a study of model and commercial fuels, Combust. Flame 158 (1) (2011) 105–116, https://doi.org/10.1016/j.combustflame.2010.07.022.
[56] S. Vemury, S.E. Pratsinis, Self-preserving size distributions of agglomerates, J. Aerosol Sci. 26 (2) (1995) 175–185, https://doi.org/10.1016/0021-8502(94)00103-6.
[57] P. Van Dongen, M. Ernst, Dynamic scaling in the kinetics of clustering, Phys. Rev. Lett. 54 (13) (1985) 1396, https://doi.org/10.1103/PhysRevLett.54.1396.
[58] K.E. Lehtinen, M.R. Zachariah, Self-preserving theory for the volume distribution of particles undergoing brownian coagulation, J. Colloid Interface Sci. 242 (2) (2001) 314–318, https://doi.org/10.1006/jcis.2001.7791.
[59] E. Otto, F. Stratmann, H. Fissan, S. Vemury, S.E. Pratsinis, Quasi-self-preserving log-normal size distributions in the transition regime, Particle Particle Syst. Char. 11 (5) (1994) 359–366, https://doi.org/10.1002/ppsc.19940110502.
[60] E. Goudeli, M.L. Eggersdorfer, S.E. Pratsinis, Coagulation of agglomerates consisting of polydisperse primary particles, Langmuir 32 (36) (2016) 9276–9285, https://doi.org/10.1021/acs.langmuir.6b02455.
[61] M. Lapuerta, R. Ballesteros, F.J. Martos, A method to determine the fractal dimension of diesel soot agglomerates, J. Colloid Interface Sci. 303 (1) (2006) 149–158, https://doi.org/10.1016/j.jcis.2006.07.066.
[62] C. Caumont-Prim, J. Yon, A. Coppalle, F.-X. Ouf, K.F. Ren, Measurement of aggregates' size distribution by angular light scattering, J. Quant. Spectrosc. Radiat. Transfer 126 (2013) 140–149, https://doi.org/10.1016/j.jqsrt.2012.07.029.
[63] G. Bushell, R. Amal, Fractal aggregates of polydisperse particles, J. Colloid Interface Sci. 205 (2) (1998) 459–469, https://doi.org/10.1006/jcis.1998.5667.
[64] J. Morán, A. Fuentes, F. Liu, J. Yon, Fracval: An improved tunable algorithm of cluster–cluster aggregation for generation of fractal structures formed by polydisperse primary particles, Comput. Phys. Commun. 239 (2019) 225–237, https://doi.org/10.1016/j.cpc.2019.01.015.
[65] M. Lattuada, H. Wu, M. Morbidelli, A simple model for the structure of fractal aggregates, J. Colloid Interface Sci. 268 (1) (2003) 106–120, https://doi.org/10.1016/j.jcis.2003.07.027.
[66] L. Ehrl, M. Soos, M. Lattuada, Generation and geometrical analysis of dense clusters with variable fractal dimension, J. Phys. Chem. B 113 (31) (2009) 10587–10599, https://doi.org/10.1021/jp903557m.
[67] L. Isella, Y. Drossinos, Langevin agglomeration of nanoparticles interacting via a central potential, Phys. Rev. E 82 (1) (2010) 011404, https://doi.org/10.1103/PhysRevE.82.011404.
[68] M. Camejo, D. Espeso, L. Bonilla, Influence of primary-particle density in the morphology of agglomerates, Phys. Rev. E 90 (1) (2014) 012306, https://doi.org/10.1103/PhysRevE.90.012306.
[69] M.L. Eggersdorfer, S.E. Pratsinis, The structure of agglomerates consisting of polydisperse particles, Aerosol Sci. Technol. 46 (3) (2012) 347–353, https://doi.org/10.1080/02786826.2011.631956.
[70] C.M. Sorensen, G.C. Roberts, The prefactor of fractal aggregates, J. Colloid Interface Sci. 186 (2) (1997) 447–452, https://doi.org/10.1006/jcis.1996.4664.
[71] M. Lapuerta, F.J. Martos, G. Martín-González, Geometrical determination of the lacunarity of agglomerates with integer fractal dimension, J. Colloid Interface Sci. 346 (1) (2010) 23–31, https://doi.org/10.1016/j.jcis.2010.02.016.
[72] H. Wu, M. Lattuada, M. Morbidelli, Dependence of fractal dimension of dlca clusters on size of primary particles, Adv. Colloid Interface Sci. 195 (2013) 41–49, https://doi.org/10.1016/j.cis.2013.04.001.
[73] L. Gmachowski, The aerosol particle collision kernel considering the fractal model of particle motion, J. Aerosol Sci. 59 (2013) 47–56, https://doi.org/10.1016/j.jaerosci.2013.02.002.
[74] P. Polovnikov, I. Azarov, M. Veshchunov, Advancement of the kinetic approach to brownian coagulation on the base of the langevin theory, J. Aerosol Sci. 96 (2016) 14–23, https://doi.org/10.1016/j.jaerosci.2016.02.006.
[75] R.I. Jeldres, P.D. Fawell, B.J. Florio, Population balance modelling to describe the particle aggregation process: a review, Powder Technol. 326 (2018) 190–207, https://doi.org/10.1016/j.powtec.2017.12.033.
[76] J. Gregory, Monitoring particle aggregation processes, Adv. Colloid Interface Sci. 147 (2009) 109–123, https://doi.org/10.1016/j.cis.2008.09.003.
[77] A.K. Singh, E. Tsotsas, A tunable aggregation model incorporated in monte carlo simulations of spray fluidized bed agglomeration, Powder Technol. 364 (2020) 417–428, https://doi.org/10.1016/j.powtec.2020.02.016.
[78] M. Bouvier, J. Yon, G. Lefevre, F. Grisch, A novel approach for in-situ soot size distribution measurement based on spectrally resolved light scattering, J. Quant. Spectrosc. Radiat. Transfer 225 (2019) 58–68, https://doi.org/10.1016/j.jqsrt.2018.12.018.
[79] H.M. Amin, W.L. Roberts, Investigating soot parameters in an ethane/air counterflow diffusion flame at elevated pressures, Combust. Sci. Technol. (2020) 1–16, https://doi.org/10.1080/00102202.2020.1715964.

[80] D. Hou, D. Zong, C.S. Lindberg, M. Kraft, X. You, On the coagulation efficiency of carbonaceous nanoparticles, J. Aerosol Sci. 140 (2020) 105478, https://doi.org/10.1016/j.jaerosci.2019.105478.
[81] E. Brugière, F. Gensdarmes, F. Ouf, J. Yon, A. Coppalle, Increase in thermophoretic velocity of carbon aggregates as a function of particle size, J. Aerosol Sci. 76 (2014) 87–97, https://doi.org/10.1016/j.jaerosci.2014.06.007.
[82] R.K. Chakrabarty, N.D. Beres, H. Moosmüller, S. China, C. Mazzoleni, M.K. Dubey, L. Liu, M.I. Mishchenko, Soot superaggregates from flaming wildfires and their direct radiative forcing, Sci. Rep. 4 (2014) 5508, https://doi.org/10.1038/srep05508.